Navier-Stokes Simulation of a Heavy Lift Slowed-Rotor Compound Helicopter Configuration

Brian G. Allan, Luther N. Jenkins, Chung-Sheng Yao,
Scott M. Bartram, Jim B. Hallissy, and Jerome Harris
NASA Langley Research Center, Hampton, VA

Kevin W. Noonan, Oliver D. Wong, Henry E. Jones, Brendon D. Malovrh, and Deane G. Reis
U.S. Army Aeroflightdynamics Directorate, NASA Langley Research Center, Hampton VA

W. Derry Mace
Sierra Lobo Inc., Hampton, VA

Time accurate numerical simulations were performed using the Reynolds-averaged Navier-Stokes (RANS) flow solver OVERFLOW for a heavy lift, slowed-rotor, compound helicopter configuration, tested at the NASA Langley 14- by 22-Foot Subsonic Tunnel. The primary purpose of these simulations is to provide support for the development of a large field of view Particle Imaging Velocimetry (PIV) flow measurement technique supported by the Subsonic Rotary Wing (SRW) project under the NASA Fundamental Aeronautics program. These simulations provide a better understanding of the rotor and body wake flows and helped to define PIV measurement locations as well as requirements for validation of flow solver codes. The large field PIV system can measure the three-dimensional velocity flow field in a $0.914\,m$ by $1.83\,m$ plane. PIV measurements were performed upstream and downstream of the vertical tail section and are compared to simulation results. The simulations are also used to better understand the tunnel wall and body/rotor support effects by comparing simulations with and without tunnel floor/ceiling walls and supports. Comparisons are also made to the experimental force and moment data for the body and rotor.

Nomenclature

CFD	Computational Fluid Dynamics
IRTS	Isolated Rotor Test System
PIV	Particle Image Velocimetry
RANS	Reynolds-averaged Navier-Stokes
SRW	Subsonic Rotary Wing
A_{rotor}	Rotor Area, $2.526\,m^2$ ($27.19\,ft^2$)
α	Fuselage Angle of Attack, $deg.$
α_s	Shaft Angle of Attack, $deg.$
θ	Blade Pitch, $deg.$
θ_0	Collective Blade Pitch, $deg.$
θ_{1S}	Longitudinal Blade Pitch, $deg.$
θ_{1C}	Lateral Blade Pitch, $deg.$
β_0	Blade Coning, $deg.$
β_{1C}	Longitudinal Flapping, $deg.$
β_{1S}	Lateral Flapping, $deg.$
C	Side Force, N
C_L	Lift Force Coef., $L/(q_\infty A_{rotor})$
C_D	Drag Force Coef., $D/(q_\infty A_{rotor})$
C_C	Side Force Coef., $C/(q_\infty A_{rotor})$
CMX	Rolling Moment Coef., $M_x/(q_\infty A_{rotor}R)$
CMY	Pitching Moment Coef., $M_y/(q_\infty A_{rotor}chord)$
CMZ	Yawing Moment Coef., $M_z/(q_\infty A_{rotor}R)$
D	Drag Force, N
L	Lift Force, N
M	Mach number
M_x	Moment in Roll, $N\text{-}m$
M_y	Moment in Pitch, $N\text{-}m$
M_z	Moment in Yaw, $N\text{-}m$
P	Pressure, Pa
q	Dynamic Pressure, $0.5\rho U^2$, Pa
R	Rotor Radius, $0.89662\,m$ ($35.3\,in$)
ψ	Azimuth Angle, deg.
u, v, w	Velocity in x, y, z directions respectively, m/s
x, y, z	Cartesian axesd, m
x_R, y_R, z_R	Cartesian axes centered about the model pitch rotation center, m
μ	Advance Ratio

Introduction

There has been a recent interest in development of a heavy lift transport rotorcraft to meet Army and Air Force mission requirements. One candidate configuration is a large slowed-rotor compound helicopter configuration with a single rotor.[1] This configuration has a conventional aircraft transport body and wing with two propulsion wing mounted engines and a large single main rotor. To better understand the characteristics of such a configuration, a 5% scale model with a four-bladed rotor was tested at the NASA Langley 14- by 22-Foot Subsonic Tunnel. In addition to the aeromechanics objectives, this wind tunnel test was used as a platform for the development of an experimental large field of view PIV flow measurement technique supported by the SRW project under the NASA Fundamental Aeronautics program. The large field of view PIV system has a maximum measurement plane size of $0.914\,m$ by $1.83\,m$, which allows many flow features to be captured at one time. To support this experimental activity, numerical simulations using the Reynolds-averaged Navier-Stokes (RANS) flow solver code, OVERFLOW, were performed. The numerical simulations and the PIV data provide a better understanding of the rotor wake flow with the simulations providing guidance on PIV measurement locations and interpretation of PIV data results. Data comparisons will also be used to develop requirements for both the PIV and numerical simulations for future code validation efforts.

The numerical simulations are also used to better understand the interaction of the rotor wake with the body and wing. Simulation results will also be used to investigate the effects of the wind tunnel floor and ceiling, as well as the model and rotor supports. Time accurate simulations using moving rigid-body rotor blades were performed and compared to the PIV results. The simulation results are compared to balance data from the body and rotor. Steady-state flow solutions for a baseline, body only case, are also compared to wind tunnel data for a body only test configuration.

Numerical Modeling Approach

Flow Solver

The flow field for the slowed-rotor was computed using the flow solver code, OVERFLOW[2,3] developed at NASA. This code solves the compressible RANS equations using the diagonal scheme of Pulliam and Chaussee.[4] The RANS equations are solved on structured grids using the overset grid framework of Steger, Dougherty, and Benek.[5] This overset grid framework allows for the use of structured grids for problems that have complex geometries and moving bodies. The numerical simulations were performed using the parallel version of the OVERFLOW code developed by Buning.[6] This code uses the Message-Passing Interface and can run on a tightly-coupled parallel machine or a network of workstations. The code distributes zones to individual processors and can split larger individual zones across multiple processors using a domain decomposition approach. The structured overset grid system was generated using the Chimera Grid Tools package.[7]

The HLLC scheme was used which is an approximate Reimann solver based on the Harten, Lax and Van Leer upwind flux algorithms for contact discontinuities. A 5th order spatial discretization using a Mapped Weighted Essentially Non-Oscillatory (WENOM) scheme was used in order to minimize the effects of numerical dissipation of the rotor vortices.[8] The Shear-Stress Transport turbulence model was used for the viscous surfaces.[9]

Time Accurate Simulations

Time accurate simulations were made using the Newton time-accurate algorithm in OVERFLOW. The physical time step was set to accurately resolve 7200 steps per revolution of the rotor blade or every $0.05°$ using 3 sub-iterations per time step. Time accurate simulations of the isolated rotor showed periodic convergence of the forces on the rotor blades by the second revolution of the rotor. As might be expected, unsteady forces on the body and support posts never reached a time periodic state. Simulations with the rotor and body with support posts were run for four revolutions to ensure that transient effects on the body and rotor were dissipated.

Grids

Isolated Rotor Grids

The isolated rotor simulations help evaluate grid density in the wake and rotor surface grids. The wake grids had a uniform spacing of $0.00635\,m$ ($0.25\,in.$) where the rotor has a main chord length of $0.0572\,m$ ($2.25\,in.$) resulting in a background spacing that is 11% of the main chord. The rotor has a tapered tip with a chord of $0.0343\,m$ ($1.35\,in.$) resulting in wake grid spacing of 19% of the rotor tip chord. The wake grid was extended 1.5 rotor radii downstream of the rotor and was 0.28 rotor radii above and below the rotor hub center. The isolated rotor simulations used the automatic background grid generation in OVERFLOW where the location and resolution of the level 1 wake grid was defined. The background grids generated by OVERFLOW are all rectilinear with isotropic spacing minimizing numerical errors.

The airfoil sections on the rotor blades had an O-type mesh with a blunt trailing edge. The mesh had 301 grid points around the airfoil with a concentration of points near the trailing edge to capture the wake of the blade. The main blade grid had 228 grid points in the spanwise direction with a spacing of $0.0051\,m$ ($0.20\,in.$) matching the wake grid spacing used in the rotor and body simulations with refined spacing near the tip and root sections. The volume grid for the blade extended 2.2 chords normal to the surface and had 81 grids points. The tip and root ends had cap grids where the tip grid had a squared end cap with slight rounding of the corners.
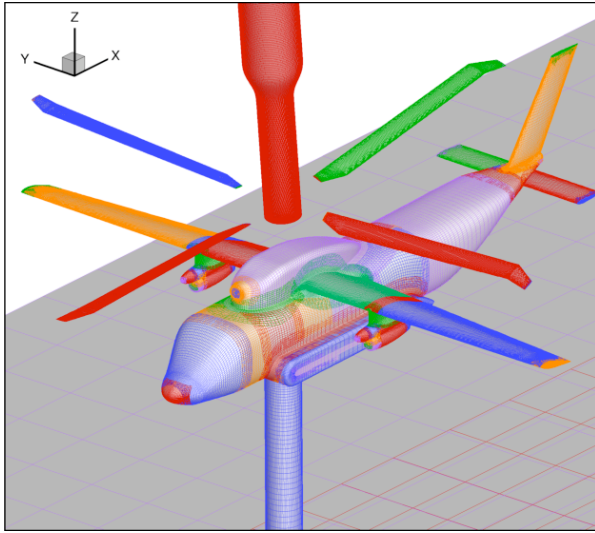
Fig. 1 Surface grids on rotorcraft vehicle, model support post, wind tunnel floor and IRTS.

Body and Rotor Grids

Figure 1 shows the overset grids for the simulation that included the body, blades, support post, tunnel floor and ceiling and the Isolated Rotor Test System (IRTS). There were 96 overset grids with a total of $127.7\,million$ grid points. Approximately 40% of the grid points were used for the rotor and rotor wake where the wake grid had isotropic spacing of $0.0051\,m$ ($0.20\,in.$), which is 15% of the tip chord and 9% of the main blade chord. Since the simulation results will be compared to flow measurements $0.3\,m$ downstream of the vertical tail, the rotor wake grid was extended beyond this PIV measurement location in order to resolve the rotor vortices at the PIV measurement plane location. A summary of the grids is given in Table 1 showing the relative computational cost for resolving the different flow regions.

The grids for IRTS represented the general shape without modeling the complex hub geometry, such as the linkage between the hub and the rotor blades. By not modeling this linkage the root section of the blades tended to produce strong vortices which could be identified downstream for simulations without the IRTS geometry.

Wind Tunnel Experiment

Wind Tunnel

The test was performed at the NASA Langley 14- by 22-Foot Subsonic Tunnel. This tunnel is a closed-circuit, single-return, atmospheric wind tunnel that can be operated in a variety of configurations including a closed or partially open test section. The test section is $4.420\,m$ ($14.50\,ft$) high by $6.629\,m$ ($21.75\,ft$) wide by $15.2\,m$ long with a maximum speed of approximately $103\,m/s$.[10] This test was conducted with the tunnel ceiling in position with the tunnel side walls removed.

Table 1 Summary of overset grids used in simulation body, post, and rotor grids.

Description	Number of Grids	Grid Points (million)
Body	68	13.8
Body Wake	1	12.5
Wing Tip Vortex	2	0.9
Rotor	12	30.5
Rotor Wake	1	22.6
Tunnel	1	6.2
Post	6	2.7
Post Wake	1	3.7
IRTS	2	14.5
IRTS Wake	2	20.3
Total	96	127.7

Blade Geometry

The rotor blades used for this test were designed to be representative of a modern rotor design. The blades were not dynamically scaled and are considered to be relatively stiff. The rotor had a radius of $0.8966\,m$ ($35.30\,in.$) with a non-uniform twist and a tapered planform, shown in Fig. 2, with swept tapered tips, a root chord of $57.15\,mm$ ($2.25\,in.$) and tip chord of $35.29\,mm$ ($1.35\,in.$) The blades used in this experiment are the same as described in the experiment of Gorton et al.[11] with the exception that the cutout and the flapping and lag hinge locations have changed. The blades and hub are described in more detail in Table 2.

Model Support

Figure 3 describes the model support post geometry and location of the body relative to the tunnel floor as well as the model center of rotation used during pitch changes. As seen in Fig. 3, the vehicle body was supported by a $0.102\,m$ ($4\,in.$) diameter circular post that was then mounted on a $0.356\,m$ ($14\,in.$) diameter circular base. The post was connected to the base by a $0.178\,m$ ($7\,in.$) diameter collar. The $0.178\,m$ diameter circular base was extended through the tunnel floor to make any height adjustments of the model. The top of the model pylon height from the floor was held fixed at $2.1336\,m$ ($84\,in.$) during the test and for model pitch changes by extending the post through the floor. For pitch changes the model was rotated about a point $2.2098\,m$ ($87\,in.$) above the floor at the centerline of the post. At the $0°$ pitch condition this rotation point is located $0.492\,m$ ($19.375\,in.$) from the nose of the model.

Rotor System

The rotor blades were powered by IRTS, which consists of a drive motor, balance, and pitch controls. IRTS is mounted through the tunnel ceiling and can move independently relative to the vehicle body allowing for varying rotor/body configurations. The rotor collective and cyclic pitch are controlled by a swash plate connected to electric actuators.[12] Figure 4 shows a diagram of the fuselage and IRTS and the rotor separation height parameter, ΔHgt

Table 2 Description of rotor blades.

Airfoil Sections		Number of blades	4
25.4-percent radius	VR-12	Pitch axis, percent of chord	25
84.9-percent radius	VR-12	Radius, in.	35.30
92.0-percent radius	SSC-A09	Solidity, thrust-weighted	0.077
100-percent radius	SSC-A09	Tip sweep angle (of 1/4 chord), deg	30
Chord, in.		Tip sweep begins, in.	32.46
25.4-percent radius	2.25	Twist, deg.	
84.9-percent radius	2.25	0-percent radius	0
92.0-percent radius	2.25	25.4-percent radius	0
100-percent radius	1.35	74.8-percent radius	-6.6
Cutout, in.	8.95	84.9-percent radius	-7.6
Flapping hindge offset, in.	2.25	92.0-percent radius	-9.5
Lag hindge offset, in.	2.25	100-percent radius	-9.5

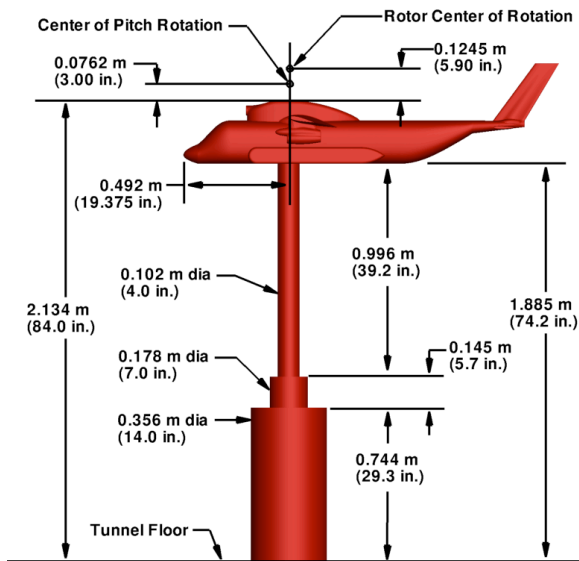**Fig. 2   Description of blade palnform. All dimensions in inches**

Fig. 3   Model support post dimensions, body height relative to the floor and model rotation center location.

Fig. 4   Diagram showing angle of attack of the model and rotor as well as the separation distance parameter ΔHgt which is the height from the top of the body pylon to the bottom of IRTS.

which was used during the test to define different rotor separation configurations. This figure also illustrates the angle of attack parameter for the fuselage, α, and the rotor shaft tilt angle, α_s, all relative to the free-stream flow.

Test Parameters

The comparison between the simulations and the experiment for the rotor and body case are made at a single test condition where most of the PIV data was taken. The test parameters for the rotor and tunnel at this condition are summarized in Table 3. The rotor conditions were set to
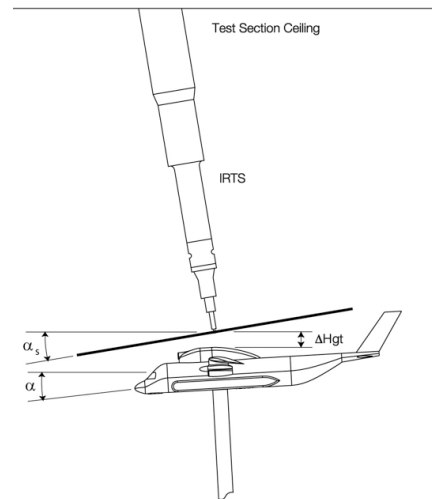
a collective of $12°$ and the cyclics were then adjusted to zero out blade flapping with respect to the rotor shaft. The rotor RPM was set for a slowed-rotor condition which resulted in an advance ratio of $\mu = 0.41$. The rotor had a shaft tilt of $-5.0°$ relative to the body and the entire vehicle was set to an angle of attack of $-0.54°$. This results in the rotor having a shaft angle, $\alpha_s = -5.54°$ relative to the wind axis.

Table 3 Test Parameters

Parameter	Value	Units	Accuracy
Free-Stream Velocity	72.0	m/s	
Hover Tip Speed, ΩR	175.6	m/s	
Rotor RPM	1870	RPM	
Advance Ratio, μ	0.41		
Fuselage Angle of Attack, α	-0.54	deg	± 0.01
Shaft Angle of Attack, α_s	-5.54	deg	± 0.01
Collective Blade Pitch, θ_0	12.0	deg	± 0.5
Longitudinal Blade Pitch, θ_{1S}	-8.7	deg	± 0.5
Lateral Blade Pitch, θ_{1C}	4.1	deg	± 0.5
Blade Coning, β_0	3.3	deg	
Longitudinal Flapping, β_{1C}	0.0	deg	
Lateral Flapping, β_{1S}	0.0	deg	
Rotor Height, ΔHgt	4.0	inch	

Large Field of View Particle Imaging Velocimetry

A large field of view PIV measurement system has been developed using a single laser light sheet and two digital imaging cameras with 11 Megapixel resolution. The PIV system is triggered by the position of the rotor to acquire instantaneous images of particles in the flow at the laser sheet location. Typically, 150 to 300 instantaneous images were processed and averaged to generate a three-dimensional flow field at a single rotor position. The setup for the rotor and body test consisted of two different sized measurement planes as shown in Fig. 5 and described in further detail by Jenkins et al.[13]

One of the PIV planes is located approximately $45\,mm$ downstream of the rotor tip path plane, upstream of the vertical tail section, with a field of view width of $0.981\,m$ and a height of $0.381\,m$. For this paper a smaller region of the measurement plane was extracted from the PIV data. The width of this plane was $0.732\,m$ and the height was $0.354\,m$ as shown in Fig. 5(b). This PIV measurement plane has a spatial resolution of $12.0\,mm$ by $12.0\,mm$. The PIV tail plane is located $0.934\,m$ from the center of pitch rotation in the streamwise direction as shown in Fig 5(a) and is located slightly above the top surface of the fuselage tail section. The top of the PIV tail plane is just above the rotor blade tip at the $0°$ degree azimuthal location. Figure 5(b) shows a view of the PIV tail plane looking upstream. This tail plane captures a spanwise area from the fuselage centerline to $0.216\,m$ on the retreating side of the rotor and $0.516\,m$ on the advancing side of the rotor. The main objective of this plane was to capture the flow upstream of the vertical tail section to better understand the flow impacting the vertical tail. The lateral extent of the PIV measurement plane on the advancing side was only able to capture part of the rotor wake from the advancing blades.

The second PIV plane is located $1.569\,m$ downstream from the center of pitch rotation as seen in Fig. 5(a). This plane is almost twice as large as the upstream PIV plane and has a width of $1.404\,m$ and a height of $0.642\,m$ with a spacial resolution of $18.6\,mm$ by $18.6\,mm$. The inten-

a) Side view of PIV tail and wake planes

b) View looking upstream at the tail plane

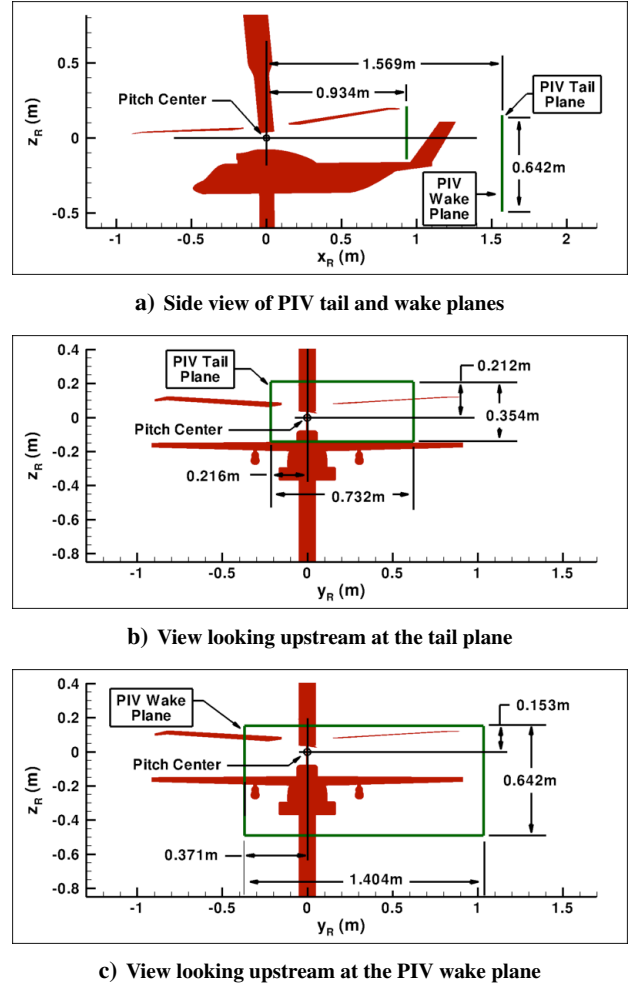**c) View looking upstream at the PIV wake plane**

Fig. 5 Location of the PIV measurement plane relative to the rotation axis.

tion of this PIV plane was to capture the fuselage, wing tip vortex and most of the rotor wake on the advancing side. This measurement plane is also centered on the advancing side of the rotor and extends $0.371\,m$ from the centerline of the model to the retreating side of the rotor and extends $1.033\,m$ on the advancing side.[13]

Results

Baseline (No Rotor)

The baseline case consisted of the vehicle fuselage and wing without the rotor and IRTS. Figure 6 shows the comparison between the baseline coefficient of lift and drag versus the angle of attack of the body for a freestream tunnel flow of $72\,m/s$. The numerical simulations for the free air case shows the baseline model without the model support post and tunnel ceiling and floor effects over a range of alpha from $-8°$ to $5°$. This comparison of the lift shows the simulation to compare well at $0°$ angle of attack but diverges for lower and higher angles of attack. Figure 6 also shows baseline simulations with the body support post as well as the tunnel ceiling and floor. In the experiment the side walls were removed and are modeled in the simulation by freestream characteristic boundary conditions. The inclusion of the post shows an angle of attack increase

a) Lift Coeficient versus Angle of Attack
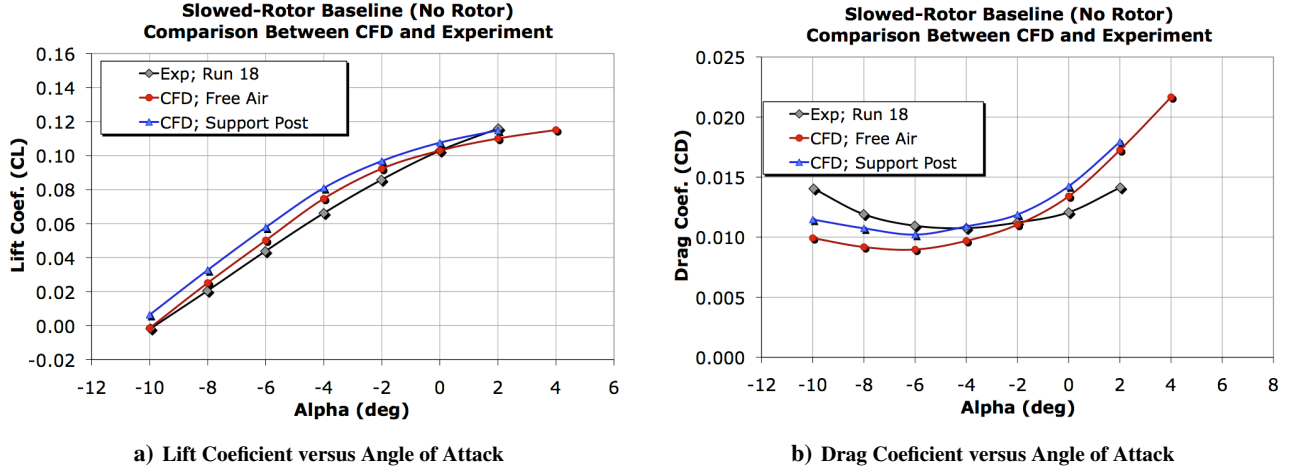

b) Drag Coeficient versus Angle of Attack

Fig. 6 A comparison of the wind tunnel balance data for the body only case with numerical simulation results. The CFD results for the free air case is the body alone without a support post or tunnel floor or ceiling. The CFD with the support post also include the tunnel floor and ceiling with free-stream boundary conditions on the side walls. All cases are run for at a freestream velocity of $72\,m/s$.

as expected since the post is causing blockage under the model diverting the flow upward, increasing the effective angle of attack on the fuselage. This shift is relatively constant over the angle of attack sweep and is approximately a shift of $0.6°$. The drag prediction is close at $-2°$ angle of attack and diverges for lower and higher angles and does not match the same trend as the experiment. Overall the baseline results with the post are showing an effective $2°$ higher angle of attack as compared to the experiment. Further investigation is needed in order to understand this difference between the experiment and CFD for the baseline configuration.

Isolated Rotor

An isolated rotor simulation was performed to evaluate the rotor without body, support and tunnel wall effects. The rotor was simulated as a rigid body that would dynamically pitch using the measured collective and cyclic angles from the experiment given in Table 3. Equation 1 was used to describe the pitching motion at the 75% radial location on the blade as a function of the azimuthal location, ψ. The blade coning angle, β_0 was modeled in the blade dynamics and the blade flapping was not modeled since it was essentially zero for the experiment. The rotor shaft angle relative to the wind axis was set to α_s and is given in Table 3 as $-5.54°$.

$$\theta(\psi) = \theta_0 + \theta_{1C}\cos(\psi) + \theta_{1S}\sin(\psi) \qquad (1)$$

The isolated rotor simulations were initially performed by turning off the viscous terms in the background grid in order to minimize the dissipation of the rotor tip vortices. This is a standard practice in these types of simulations, however, when this was done using the high order numerical scheme with low dissipation, a vortex instability was observed 1.5 rotor radii downstream of the rotor and can be seen in Fig. 7(a). This instability seems to be triggered by the interaction of the wake generated by the rotor root vortices and the tip vortex as it is advected downstream. When

using the standard second order scheme and an inviscid wake, these vortices are dissipated and do not result in this type of instability. Therefore, this instability was caused by a combination of the 5th-order-scheme low dissipation without viscous effects and the interaction of the root vortices with the tip vortex. Turning on the viscous terms with the high-order numerical scheme suppressed this tip vortex instability as shown in Fig. 7(b). With the viscous terms turned on in the background grid, the root tip vortices were diminished, which is speculated to have caused the tip vortex instability. A second effect is that by turning on the viscous terms the overall dissipation is increased, which can also add to the stability of the tip vortex. Overall this isolated rotor simulation using the high-order scheme showed good preservation of the tip vortices to the downstream location where the PIV measurements were made.

The forces and moments for the isolated rotor case are compared to the experiment in Fig. 8. This comparison shows that the total lift of the rotor is about 41% higher than the mean lift measured in the experiment. The rotor simulation also has a much lower drag than measured by the experiment. In the experiment the hub region was also part of the rotor loads and has not been subtracted. It is speculated that the large difference in the drag between the experiment and CFD simulations is a result of the hub drag. The drag force from the rotor hub also contributes to the higher pitching moment measured in the experiment as compared to the isolated rotor case. The computed yawing moment compares well with experiment. The experimental rolling moment is nearly zero, as the rotor blades are free to flap in the experiment. The CFD rolling moment is positive, as the lift is higher on the advancing side of the rotor in the numerical simulation where the blades are not free to flap.

An analysis was made for the isolated rotor using the Comprehensive Analytical Model of Rotorcraft Aerodynamics and Dynamics (CAMRAD-II) software developed

a) Inviscid background grids

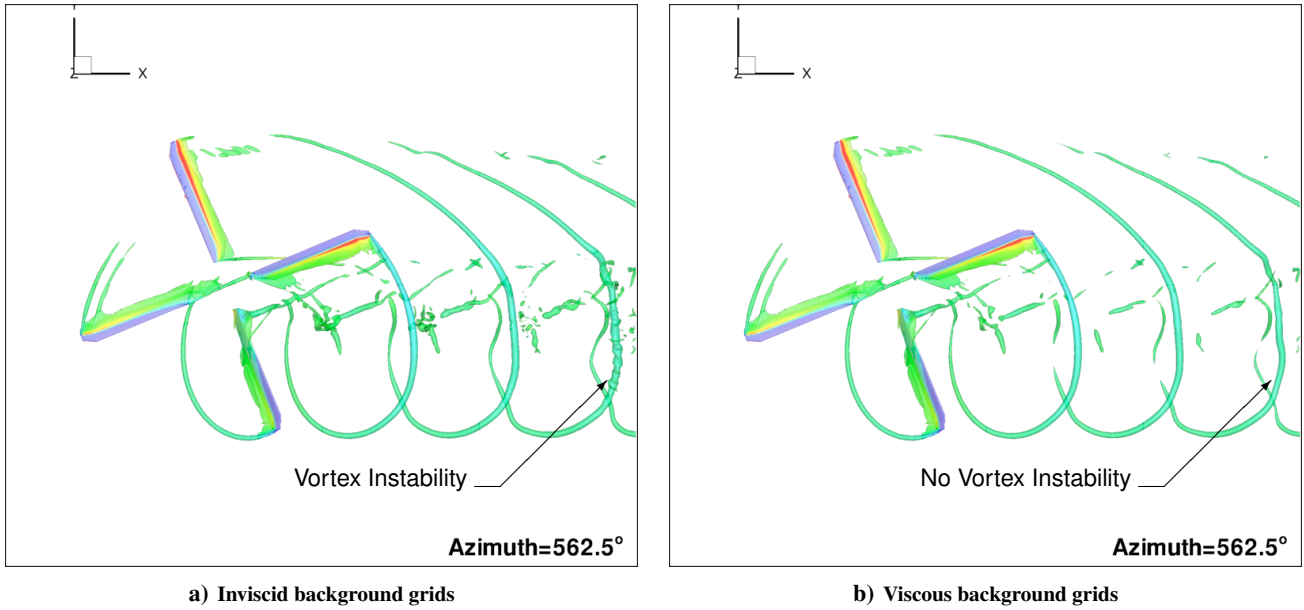**b) Viscous background grids**

Fig. 7   Simulation of the isolated rotor comparison between (a) inviscid background grids and (b) viscous background grids with SST turbulence model turned on. Plots are showing iso-surface contours of vorticity magnitude shaded by the coefficient of pressure. Note the vortex instability on the downstream tip vortex for the inviscid simulation as compared to the simulation with viscous model.

by Johnson.[14] CAMRAD-II was run using the same rigid rotor assumption with the same collective, cyclic and coning parameter values as used in the CFD simulation. This analysis resulted in a lift coefficient of $C_L = 0.108$ as compared to 0.103 from the numerical simulations of the isolated rotor. A simple uniform mass structural model was used to evaluate the effect of the blade elasticity on the rotor loads using CAMRAD-II. This analysis resulted in a $C_L = 0.103$ which suggests that the elasticity of the blades for this condition has very little effect on the lift forces and that the assumption of a rigid rotor for this condition may be valid. CAMRAD-II was also used to find a trimmed condition were the rotor thrust was matched to the experiment. This resulted in a collective of $9.7°$, a lateral cyclic of $2.7°$, a longitudinal cyclic of $-8.8°$ and a coning angle of $3.2°$. From the trimmed CAMRAD-II case a decrease of $2.3°$ in the collective and a $1.4°$ reduction in the lateral cyclic was required to match the rotor thrust. The uncertainty in the measured collective and lateral angles is $\pm 0.5°$, which is not large enough to cause the present lift discrepancies. In order to evaluate this difference in the lift, simulations including the body and IRTS as well as the tunnel floor and ceiling were performed.

Rotor and Body

Time accurate simulations were performed with the body, rigid rotor blades, and IRTS. This simulation also modeled the body support post and tunnel floor and ceiling and used free-stream characteristic boundary conditions on the tunnel side walls. The conditions were set to match the test parameters given in Table 3 where the PIV data was obtained. Figures 9 and 10 are plots of iso-surface contours of the vorticity magnitude shaded by the coefficient of pressure for a blade one azimuth angle of $1521°$. The

simulation started from a steady-state flow solution where the time-accurate simulations began at a blade one azimuth angle of $0°$. Therefore a blade one azimuth of $1521°$ is equivalent to four revolutions of blade one with the blade at an azimuth angle of $81°$. Figure 9 is a perspective view of the iso-surface vorticity magnitude contours and Fig. 10 is a side view of the body and rotor with body support and IRTS. These two figures provide a general sense of the complex interaction of the wake flow from IRTS on the rotor and the interaction of this combined wake on the vertical tail. The rotor tip vortices can be identified in Fig. 9 and are more prominent on the retreating side of the rotor. This figure also shows the rotor tip vortex breaking up in the wake region of IRTS. A high pressure region can also be seen in Fig. 9 where the rotor blade is hitting one of the tip vortices generated by preceding blade.

Rotor Loads

The loads on the rotor are compared to experimental balance data in Fig. 8 for the body and rotor with and without IRTS. The simulation with the body and IRTS predicts a 4% drop in the mean rotor lift coefficient to $C_L = 0.098$ from the isolated rotor value of $C_L = 0.103$ but still shows a mean C_L which is 36% higher than the experimental value of 0.072. The total rotor lift prediction with IRTS also shows large spikes every $90°$ at the $0°$ blade location as a result of the interaction of the rotor with the wake of IRTS. A comparison of the predicted total rotor loads with the experiment show similar differences in the drag and pitching moment, as was seen in the isolated rotor case. Again, this difference is at least partially attributed to the fact that the experiment includes the forces on the hub region adding to the drag and pitching moment where the
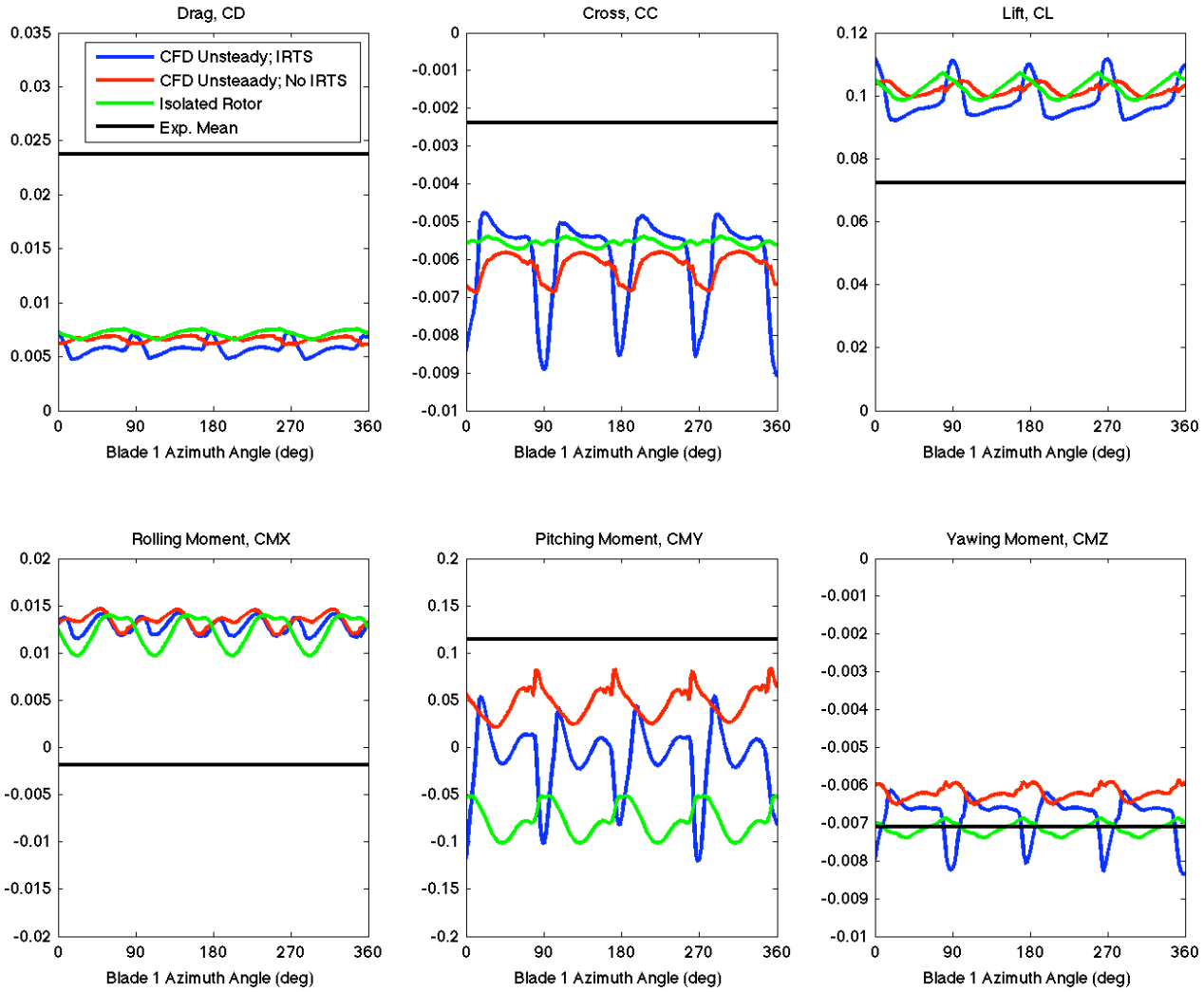
Fig. 8 A comparison of the wind tunnel balance data (black line) to the CFD simulations for the isolated rotor in free air (green line), the rotor, body and support post with IRTS (blue line) and without IRTS (red line).

simulations do not. The body and rotor simulation with IRTS does show a higher pitching moment as compared to the isolated rotor case but still below the pitching moment of the experiment.

Figure 8 also shows the loads from a simulation for the rotor and body without IRTS. A comparison of the simulations with and without IRTS can be used to better understand the effect of IRTS on the total rotor loads. The numerical simulations predict that IRTS decreases the mean rotor lift coefficient by 4% from a C_L of 0.102 without IRTS to 0.098 with IRTS. The simulations are also showing that IRTS has a significant effect on the pitching moment changing CMY from a value of 0.048 without IRTS to a -0.012 with IRTS. The simulation with IRTS also predicts a higher harmonic on the pitching moment as compared to the simulations without IRTS.

PIV Streamwise Vorticity Comparisons

Comparisons of the streamwise vorticity are made between the numerical simulation with the body, rotor and IRTS to the PIV measurements at the two locations upstream and downstream of the tail as shown in Fig. 5. Comparisons for a blade azimuth of $45°$ and $90°$ to the PIV measurements downstream of the vertical tail are shown in Fig. 11. These PIV measurements capture the blade tip vortex at the top of the frame with the wing tip vortex at the right center as well as horizontal tail vortices. The rotor tip vortices from a wake age of $90°$ can also be identified in both the PIV and CFD simulations. The simulation for the $45°$ blade location shows the strong tip vortex at the top of the frame at $z_R = 0.128\,m$ where the same vortex for the PIV is at $z_R = 0.0.097\,m$. This tip vortex from the simulation is also shifted to the right at $y_R = 0.35\,m$ compared to the vortex position in the PIV data at $y_R = 0.26\,m$. A comparison of the wing tip vortex center also shows a shift to the right in the simulation as compared to the PIV measurements. Inspection of the horizontal tail vortices shows a good comparison between the CFD and PIV.

Likewise, Fig. 11(b) is a comparison of the streamwise vorticity for a blade azimuth angle of $90°$. This comparison shows similar features as the $45°$ case with a more circular
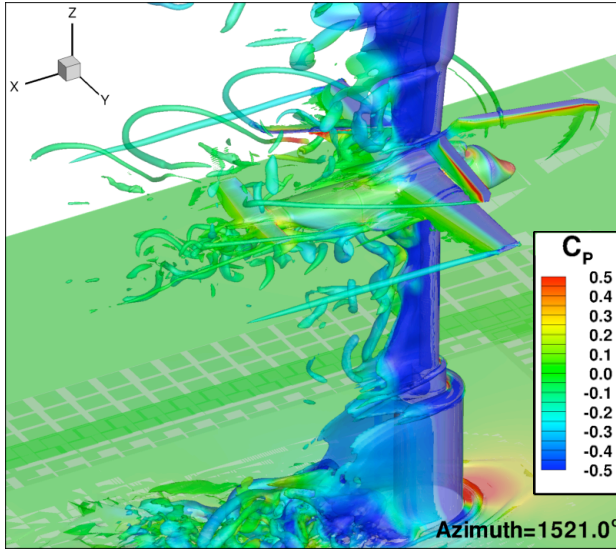
Fig. 9 Iso-surfaces for a constant vorticity magnitude shaded by the static pressure for the numerical simulation showing the complex flow generated by the rotor, fuselage and fuselage support structure and IRTS.
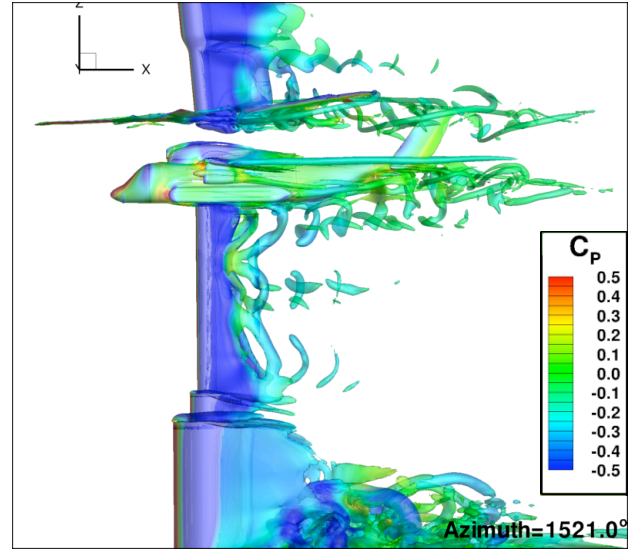

Fig. 10 Sideview of the iso-surfaces for a constant vorticity magnitude shaded by the static pressure for the numerical simulation showing the complex flow generated by the rotor, fuselage and fuselage support structure and IRTS.

blade tip vortex at the top of the frame. A comparison of the vortex locations shows the rotor tip vortex in the CFD at $z_R = 0.0.085\,m$ as compared to the experiment, which is higher at $z_R = 0.0.115\,m$. Since the rotor lift is higher in the CFD it is expected that the rotor vortices would be located vertically higher in the experiment as compared to the CFD. Therefore the tip vortex for the blade azimuth angle of $90°$ is consistent with the difference in rotor lift. However, the tip vortex for the $45°$ case is not consistent with the rotor lift as the CFD is predicting the vortex at a higher vertical location than the experiment. This difference in the $45°$ azimuth case is thought to be related to the interaction of the tip vortex with the wake of IRTS. In this location the CFD may not be properly modeling the wake from the IRTS, causing the location of the tip vortex to be higher than expected.

A comparison of the streamwise vorticity upstream of the tail is shown in Fig. 12. This figure shows a better prediction of the location of the blade tip vortices than the comparison downstream of the tail. This PIV measurement plane is $45\,mm$ downstream of the blade at $y_R = 0$ and has a shorter wake age as compared to the downstream PIV comparisons. Therefore the location of the tip vortex near $y_R = 0$ for the upstream PIV frame is dominated by the location of the blade tip. As the vortices move away from $y_R = 0$ the wake age becomes longer and the location of the tip vortex is influenced by the rotor downwash.

Figure 12(a) shows the streamwise vorticity for a blade azimuth of $48°$ and captures a tip vortex and blade wake vortex sheet. This figure also captures the blade wakes from previous blades and compares well in location and shape. Note that for this location the downstream PIV camera was obstructed by the vertical tail, resulting in a triangular blank region in the lower left of the PIV frame.

Figure 12(b) shows the streamwise vorticity for a blade azimuth of $6°$ and captures two blade tip vortices. Note that the blade tip vortex at the upper left of the frame is crossing the frame at a skewed angle resulting in an oval shape. This vortex can be seen in the PIV data at a lower z_R location but with the same shape. The numerical simulations also show wake vortices at the centerline of the PIV frame between $y_R = -0.2$ and 0.20, which may be attributed to the fact that the PIV measured data is averaged and the CFD is an instantaneous snapshot in time. This averaging of the PIV will smear out the unsteady wake flow behind IRTS

Vortex Core Comparisons

A comparison of the vortex core properties is shown in Fig. 13 for the blade tip vortex in Fig. 12(a) at the $48°$ azimuth blade location for a constant z_R value. The streamwise vorticity across the vortex core is compared in Fig. 13(a) for the CFD simulation and the PIV measured data. This comparison shows good agreement in the y_R location with the CFD having a higher peak streamwise vorticity as compared to the experiment. This should be expected since the simulation was matching the collective and cyclics resulting in a higher rotor thrust than the experiment. This plot also shows that the PIV data has sufficient resolution to resolve the blade vortex at this location. Figure 13(b) compares the vertical velocity across the vortex for a constant z_R and shows higher peaks in the CFD with the same slope in the vertical velocity across the vortex core. The streamwise velocity comparison in Fig. 13(c) shows that the CFD has a much larger velocity deficit as compared to the experiment. This difference in the streamwise velocity profile may be a result of the PIV being averaged resulting in a smearing of the streamwise velocity profile minimum. It may also be attributed to the

difficulty of keeping particles at the center of the vortex, which are needed to make good PIV measurements. The spanwise velocity profile comparison in Fig. 13(d) does not compare well but may also be a result of the averaging of the PIV frames versus the instantaneous shopshot from the CFD.

PIV Velocity Comparisons

Comparisons of the velocity components between the PIV and simulations are made in Figs. 14 through 17. These plots compare the streamwise, vertical, and spanwise velocity components ahead and behind the tail. Figure 14 compares the velocity components ahead of the tail for a blade azimuth of $6°$. This figure reveals a much larger velocity deficit in the streamwise velocity component at the centerline ($y_R = 0$) as compared to the numerical simulations. The spanwise velocity comparison for the $6°$ case, Fig. 14(b), reveals a large positive spanwise flow for the simulation as compared to the PIV. Likewise, the vertical velocity for the $6°$ case, Fig. 14(c), has a higher vertical velocity in the rotor wake region for the CFD as compared to the PIV at the top center of the PIV frame. The velocity contours for the $48°$ blade azimuth case shows similar trends as the $6°$ case. Figure 15(a) shows the PIV to have a larger streamwise velocity deficit at the centerline of the frame on top of the tail section. The vertical velocity in Fig. 15(c) shows the simulation to have a large down flow velocity region as compared to the PIV. Some of the differences may be explained by PIV time averaging as compared to the CFD, which is instantaneous. Therefore the CFD contours are showing the large eddies for that instant of time where they could be averaged out for the PIV contours.

Velocity comparisons for the PIV data downstream of the vertical tail are made in Figs. 16 and 17. Like the comparisons ahead of the tail, the streamwise velocity is showing a large deficit at the centerline for the PIV data as compared to the CFD. The spanwise flow velocity comparison is showing the CFD to have regions with larger spanwise velocities as compared to the PIV but this may be a result of the PIV averaging. The vertical velocity comparison for the PIV data downstream of the tail are comparable with the CFD having some regions with larger vertical velocities.

Summary

Navier-Stokes simulations of a heavy lift slowed-rotor compound helicopter configuration have been performed. Baseline (no rotor) simulations have been performed with and without the body support post and tunnel floor and ceiling effects. Overall the baseline comparisons did not match with the CFD free air simulations and over predicted the lift coefficient as compared to the experimental data. The free air simulations showed good prediction of the lift at $0°$ angle of attack with a maximum difference of 12% at $-4°$ angle of attack. Including the tunnel floor and ceiling with model support shifted the lift curve slope up as

the post blockage increased the effective angle of attack by $0.6°$. This difference in lift is showing the CFD to have an effective increase of $2°$ angle of attack as compared to the experimental data. Further investigation is required as to why there is such a large difference in the baseline performance predictions.

A simulation of the slowed-rotor compound helicopter configuration was performed modeling the fuselage support post and IRTS. This simulation was compared to the rotor balance data from the experiment and PIV flow field measurements upstream and downstream of the vertical tail. The rotor simulations were made by matching the collective and cyclics measured in the experiment and assuming a rigid rotor blade. The numerical simulations showed the rotor lift to be 36% higher than the experiment. An isolated rotor simulation was also performed and compared to a CAMRAD-II rigid rotor analysis resulting in the same lift and drag forces predicted by the CFD simulations. CAMRAD-II was also used to evaluate the effects of an elastic rotor blade using a simple uniform mass structural model. This CAMRAD-II prediction had a less than 1% decrease in the lift for the elastic rotor blade analysis suggesting that the blade elasticity is not contributing to the difference in lift. A CAMRAD-II analysis was made by trimming the rotor to match the rotor thrust showing that a decrease of $2.3°$ in the collective was needed to match the rotor thrust. The uncertainty of the collective measurement is $\pm 0.5°$ suggesting that the measurement of the collective does not account for the difference in the rotor thrust. The numerical simulations did model the floor and ceiling but did not accurately model flow on the sides where the side walls have been removed. Further investigation is required to determine why there is this difference in rotor lift.

Comparisons of the streamwise vorticity were made between the CFD simulations and PIV measurements upstream and downstream of the tail and showed good agreement with the overall vortex features. Some of the CFD vortices had differences in the location of the blade and wing tip vortices. Some of these differences are attributed to not matching the rotor thrust of the experiment and others are thought to be related to not capturing the wake effects of IRTS well in the numerical simulations. A comparison of the streamwise vorticity profile through one of the blade tip vortices showed good agreement between the CFD and PIV with the CFD showing a higher peak, which is attributed to the higher rotor lift. This comparison also showed that the PIV had good resolution for the blade tip vortex and that the vertical velocity profile matched the slope of the velocity profile through the vortex with the CFD having higher peaks.

A comparison of the velocity contours showed that the PIV had a much larger flow deficit at the centerline of the vehicle behind IRTS as compared to the CFD. Not matching the rotor thrust may be a contributing factor for not comparing well in this region. However a second possibility could be that the simulation needs to model more of the geometry in the hub region where the linkage between

the hub and blades are not currently modeled. The CFD simulations are also not modeling the rotational effects of the hub on the wake flow. There is also a difference in how the PIV is averaging the flow field, which is different than the instantaneous snapshot of the CFD. This difference can be a problem in regions where there is flow separation with large eddies like behind IRTS. The CFD can be averaged in the same sense as the PIV but this would require many frames and it is unknown how many frames are needed to converge to an average flow field.

Acknowledgment

References

[1]Johnson, W. and Floros, M. W., "Stability Analysis of the Slowed-Rotor Compound Helicopter Configuration," Tech. rep., Annual American Helicopter Society, June 2004.

[2]Buning, P. G., Jespersen, D. C., Pulliam, T. H., Klopfer, W. M., Chan, W. M., Slotnick, J. P., Krist, S. E., and Renze, K. J., "OVERFLOW User's Manual Version 1.8m," Tech. rep., NASA Langley Research Center, 1999.

[3]Jespersen, D., Pulliam, T., and Buning, P., "Recent Enhancements to OVERFLOW," AIAA paper 97–0644, January 1997.

[4]Pulliam, T. H. and Chaussee, D. S., "A Diagonal Form of an Implicit Approximate-Factorization Algorithm," *Journal of Computational Physics*, Vol. 39, February 1981, pp. 347–363.

[5]Steger, J. L., Dougherty, F. C., and Benek, J. A., "A Chimera Grid Scheme," *Advances in Grid Generation*, edited by K. N. Ghia and U. Ghia, Vol. 5 of *FED*, ASME, New York, NY, 1983.

[6]Murphy, K., Buning, P., Pamadi, B., Scallion, W., and Jones, K., "Status of Stage Separation Tool Development for Next Generation Launch Technologies," AIAA paper 04–2595, June 2004.

[7]Chan, W. M. and Gomez, R. J., "Advances in Automatic Overset Grid Generation Around Surface Discontinuities," AIAA Paper 99–3303, July 1999.

[8]Nichols, R. H., "Algorithm and Turbulence Model Requirements for Simulating Vortical Flows," AIAA Paper 08–0337, January 2008.

[9]Menter, F., "Improved Two-Equation Turbulence Models for Aerodynamic Flows," NASA/TM 1992–103975, 1992

[10]Gentry, G. L., Quinto, P. F., Gatlin, G. M., and Applin, T., Z., "The Langley 14- by 22-Foot Subsonic Tunnel: Description, Flow Characteristics, And Guide For Users," NASA/TP 1990–3008, 1990.

[11]Gorton, S. A., Berry, J. D., Hodges, W. T., and Reis, D., "Flow Environment Study Near the Empennage of a 15-Percent Scale Helicopter Model," NASA/TP 2000–210085, 2000.

[12]Phelps, A. E. and Berry, J. D., "Description of the Army's 2-Meter Rotor Test System," NASA/TM 1987–87762, 1987.

[13]Jenkins, L. N., Yao, C. S., Bartram, S., Harris, J., Allan, B., Wong, O., and Mace, D., "Development of a Large Field-of-View PIV System for Rotorcraft Testing in the 14x22 Subsonic Wind Tunnel," Tech. rep., 65th Annual American Helicopter Society Forum, May 2009.

[14]Johnson, W. "CAMRAD II, Comprehensive Analytical Model of Rotorcraft Aerodynamics and Dynamics," Johnson Aeronautics, Palo Alto, California, 1992-1997.
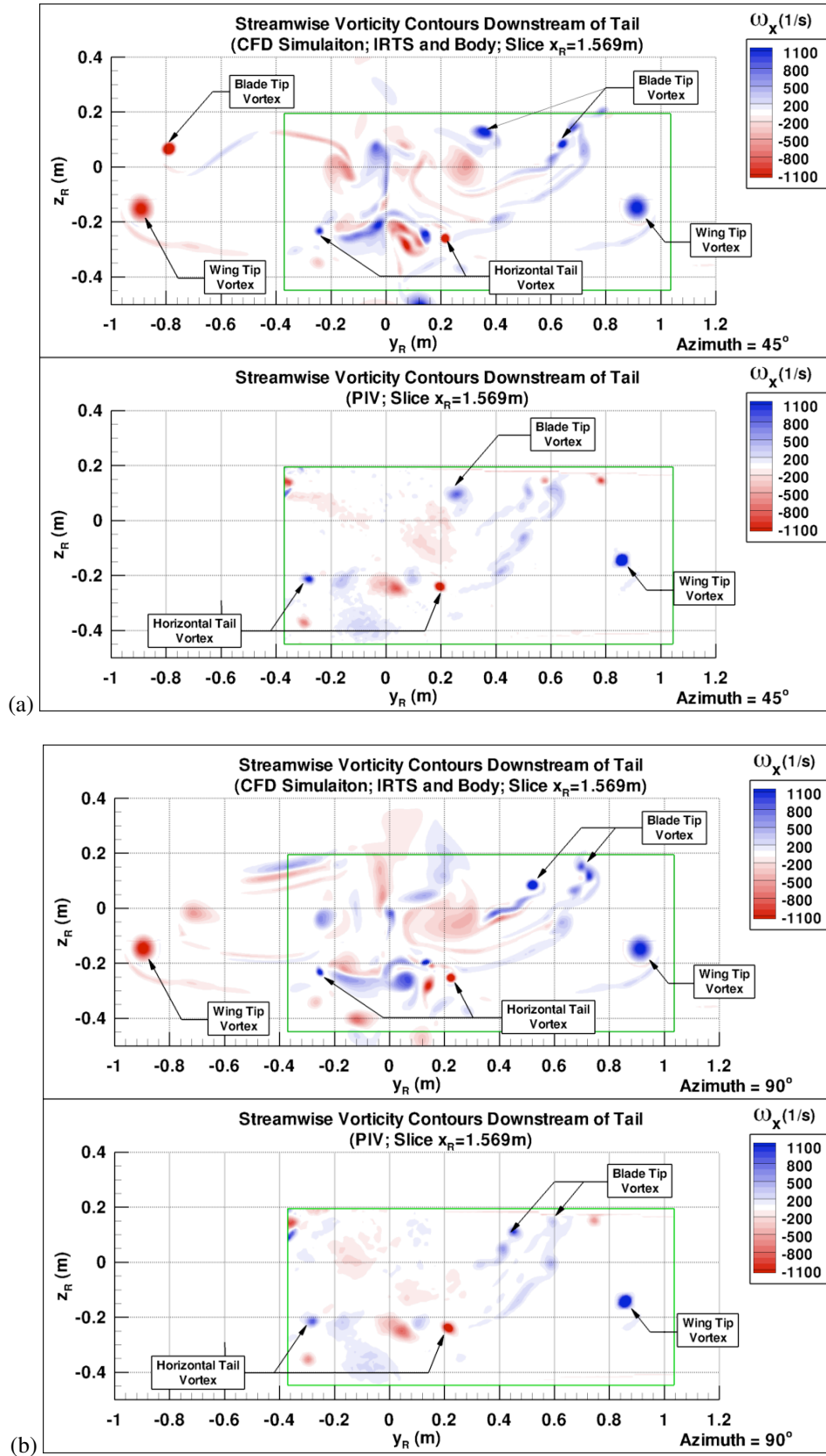
Fig. 11 A comparison of the wind tunnel PIV measurements in the wake of the rotor and body downstream of the tail to the numerical simulation results modeling the body support post and IRTS.
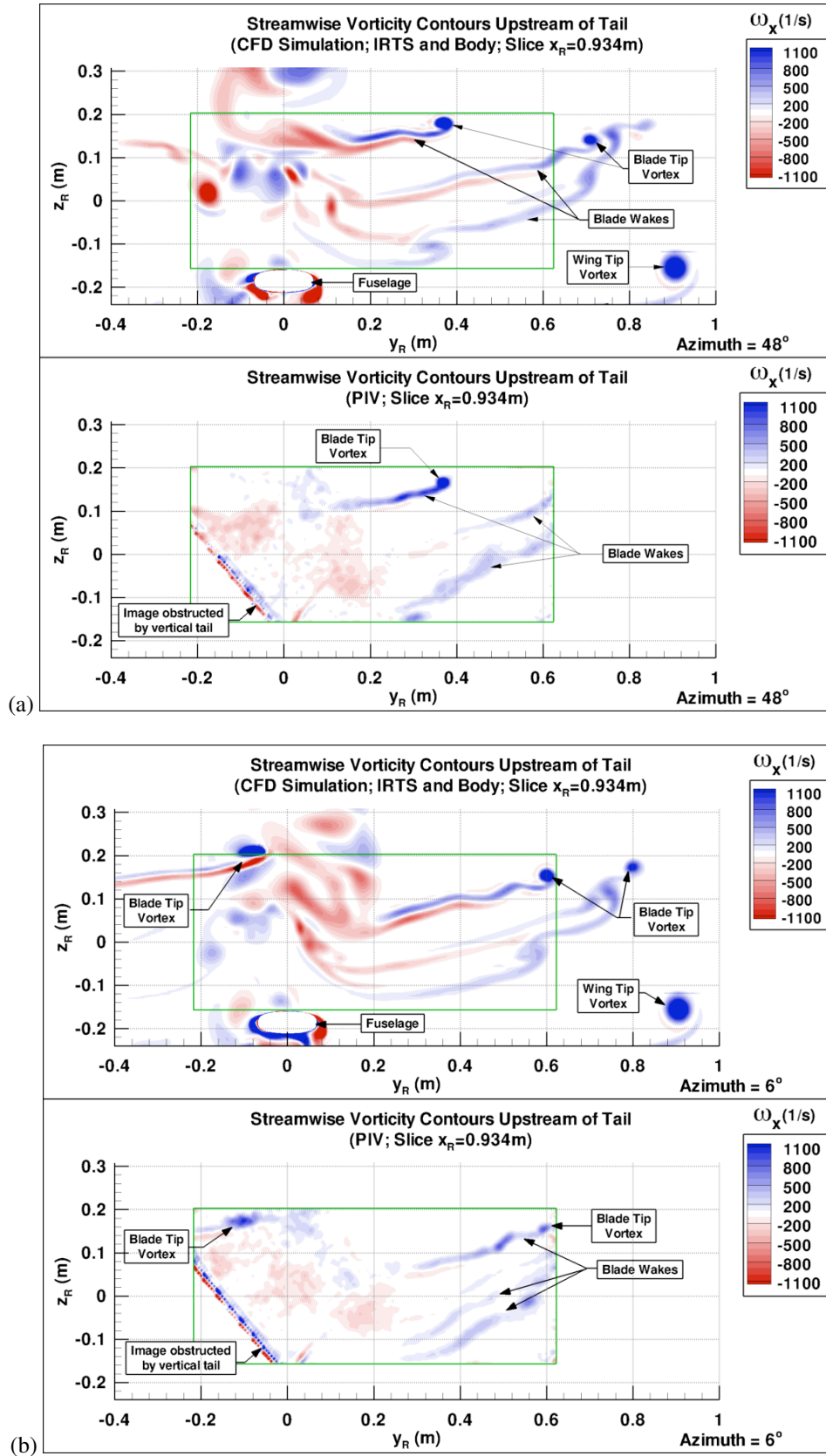
Fig. 12   A comparison of the wind tunnel PIV measurements in the wake of the rotor and body upstream of the tail to the numerical simulation results modeling the body support post and IRTS.
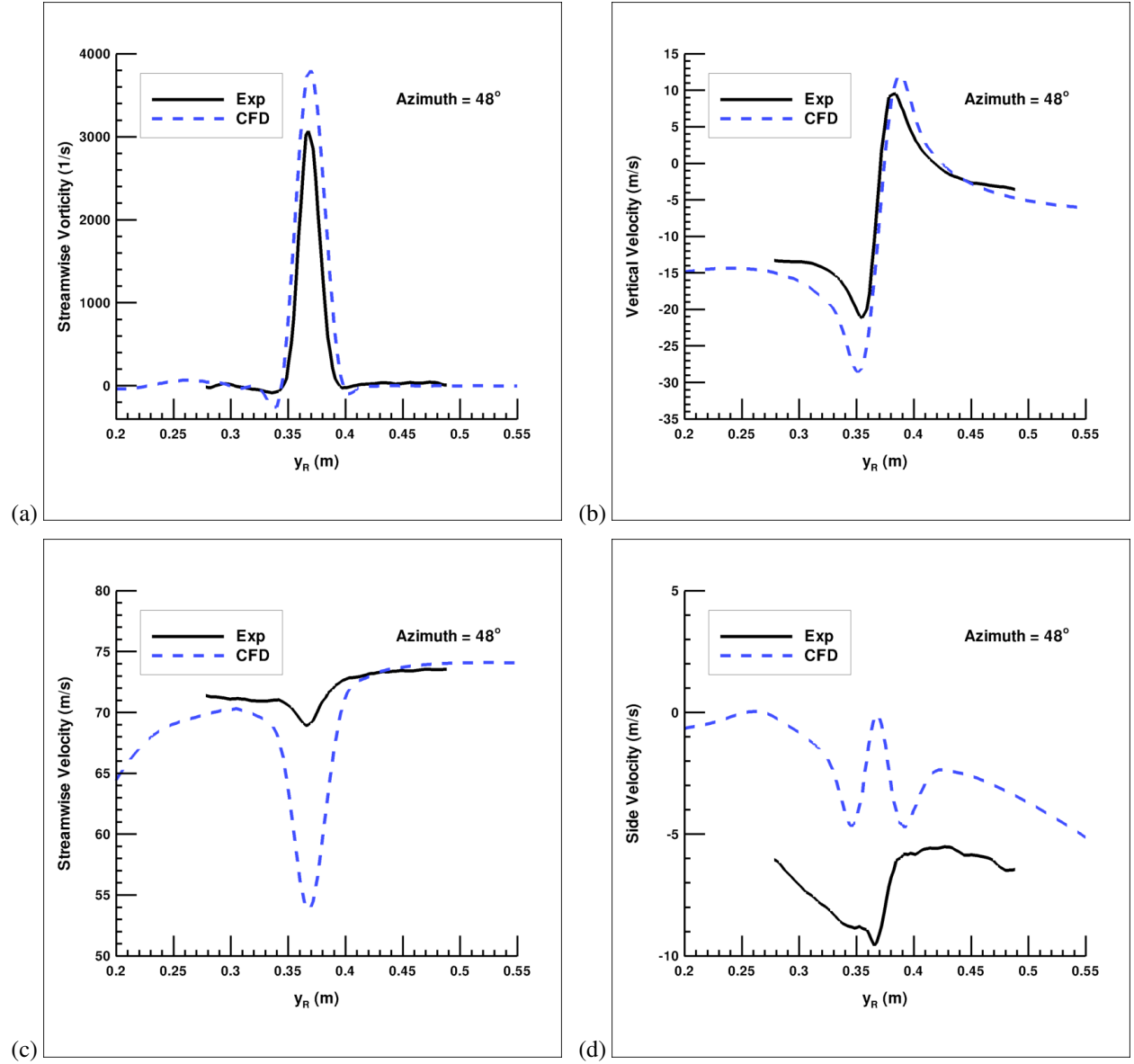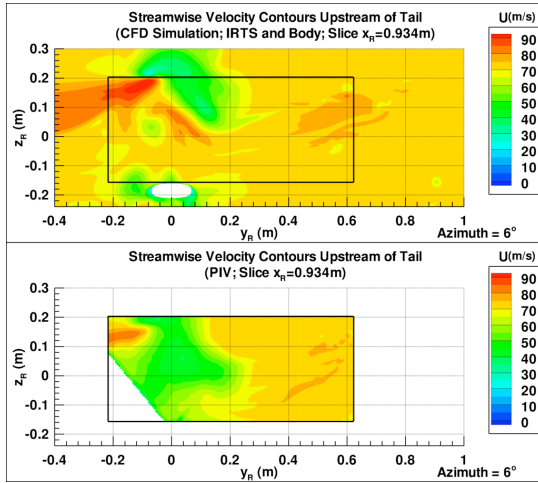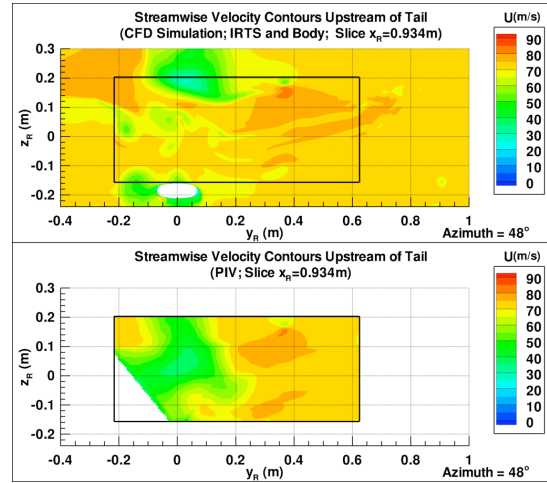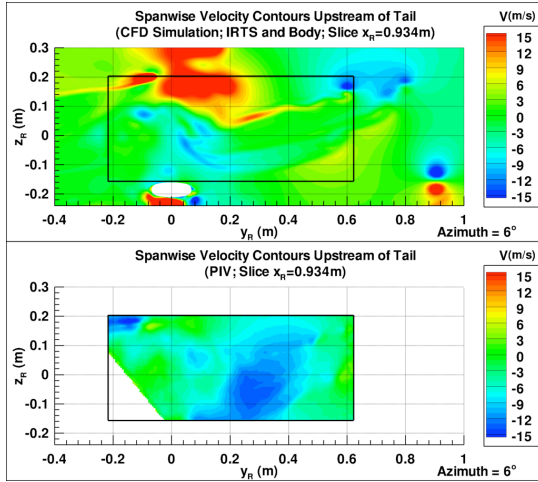
Fig. 13 A comparison of the PIV measurements and the CFD for the tip vortex at the 48° azimuth blade location for the PIV plane at $x_R = 0.934\,m$ just upstream of the vertical tail . The comparison is made using the simulation with the rotor and body and IRTS.

(a) Streamwise Velocity

(b) Spanwise Velocity

(c) Vertical Velocity

Fig. 14 **A comparison of the PIV measurements and the CFD velocity contours ahead of the vertical tail for a blade azimuth of $6°$. The CFD simulation included the rotor, body, body support and IRTS.**
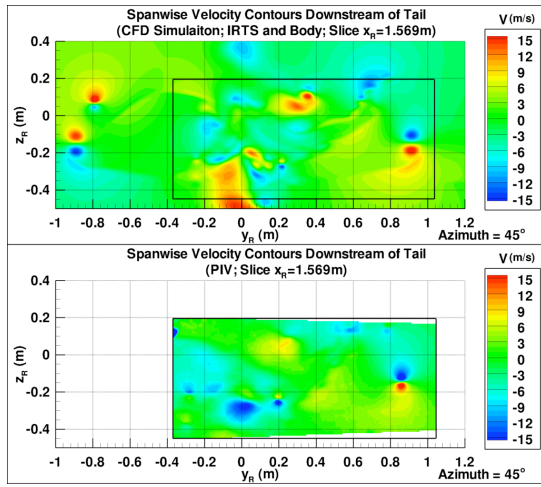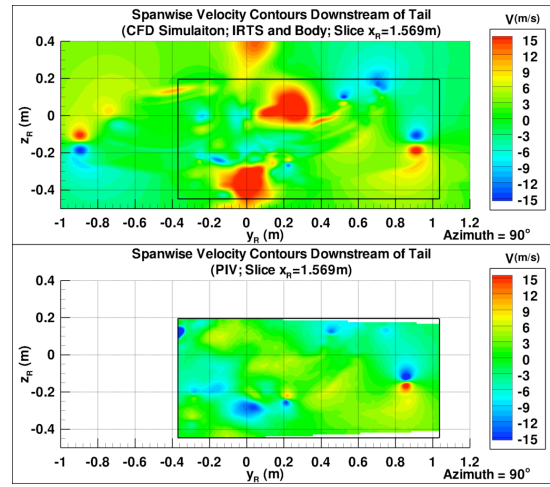

(a) Streamwise Velocity

(b) Spanwise Velocity

(c) Vertical Velocity

Fig. 15 **A comparison of the PIV measurements and the CFD velocity contours ahead of the vertical tail for a blade azimuth of $48°$. The CFD simulation included the rotor, body, body support and IRTS.**
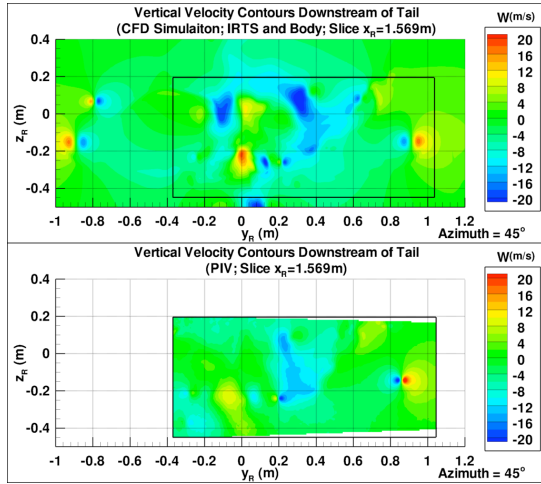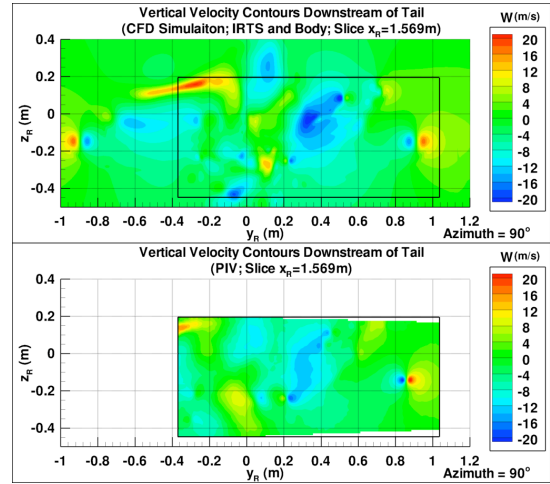
(a) Streamwise Velocity

(a) Streamwise Velocity

(b) Spanwise Velocity

(b) Spanwise Velocity

(c) Vertical Velocity

(c) Vertical Velocity

Fig. 16   A comparison of the PIV measurements and the CFD velocity contours downstream of the vertical tail for a blade azimuth of $45°$. The CFD simulation included the rotor, body, body support and IRTS.

Fig. 17   A comparison of the PIV measurements and the CFD velocity contours downstream of the vertical tail for a blade azimuth of $90°$. The CFD simulation included the rotor, body, body support and IRTS.